15

# Correlative extreme ultraviolet, ultraviolet and optical microscopy based on a specular microscope with axial tomography

© I.V. Malyshev,[1] D.G. Reunov,[1] N.I. Chkhalo,[1] M.N. Toropov,[1] A.E. Pestov,[1] V.N. Polkovnikov,[1] A.K. Chernyshov,[1] R.S. Pleshkov,[1] E.P. Kazakov,[2,3] S.V. Lavrushkina,[2] S.A. Golyshev,[2] A.D. Pospelov,[4] O.M. Shirokova[5]

[1] Institute of Physics of Microstructures, Russian Academy of Sciences,
603950 Nizhny Novgorod, Russia
[2] A.N. Belozersky Scientific Research Institute of Physico-Chemical Biology,
119234 Moscow, Russia
[3] Faculty of Biology, Lomonosov Moscow State University,
110234 Moscow, Russia
IFx3XeLobachevsky State University,
603022 Nizhny Novgorod, Russia
[5] Privolzhsky Research Medical University,
603005 Nizhny Novgorod, Russia
e-mail: reunov_dima@ipmras.ru

*Received May 6, 2024*
*Revised May 6, 2024*
*Accepted May 6, 2024*

The work is devoted to the use of a mirror extreme ultraviolet microscope with a magnification of 46 times and a resolution of up to 140 nm for studying samples at three wavelengths: 13.84 nm, 200 nm and 535 nm is considered. The ability to see one area of a sample at different wavelengths provides additional information about its structure. The choice of wavelength occurs by changing sources: LED or gas laser-plasma source, as well as input-output of a multilayer filter that cuts off everything except 13.84 nm. For three-dimensional reconstruction, the sample was scanned along the optical axis using a piezo actuator. In reconstructing images from tomographic data, a point spread function is used, modeled on the basis of aberrations measured on an interferometer.

**Keywords:** extreme ultraviolet microscopy, ultraviolet microscopy, axial tomography, electron microscopy, soft x-ray microscopy.

DOI: 10.61011/TP.2024.08.59008.156-24

## Introduction

A detailed study of cells in modern biology and medicine requires acquiring their image with a nanometer resolution [1]. Optical microscopy operating in visible light does not allow direct examination of the nanostructure of living cells with details less than 200 nm due to diffraction blurring [2]. Various methods for increasing the resolution of optical microscopy by staining organelles or proteins [3] allow bypassing the diffraction limit and achieving a resolution of tens of nanometers. However, organelle staining in isolation from the environment makes it difficult to understand the processes occurring in cells.

The electron microscopy has a high spatial resolution, up to nanometers [4]. However, to conduct such studies, samples must be fixed chemically or by freezing and sections 100–500 nm thick must be made, i. e. this method is destructive and cannot be used to study living cells [5]. The atomic force and scanning tunneling microscopy allow studying only the surface of the samples.

On the other hand, soft X-ray microscopy (SX-microscopy) has been developing for more than thirty years in the spectral region of the „water transparency window“, wavelengths of 2.3−4.4 nm [6–10], of the „carbon transparency window, at wavelengths of 4.5−6 nm“ [11], as well as in the extreme ultraviolet (EUV) region at wavelengths of 13.4−13.8 nm [12–16]. This method has the following main advantages in the „water window“

- short wavelength in the diffraction limit ensures nanometer spatial resolution;
- natural absorption contrast (by an order of magnitude or more) between carbon-containing structures and water makes it possible to examine samples without using contrasting and/or fluorescent substances;
- relatively high transmittance and virtually no scattering of radiation makes it possible to study cells and tissue sections up to 10−15 $\mu$m thick in their native, potentially alive state;
- sample preparation is significantly simplified in comparison with existing methods of nanoscopy.

3*D*-images of frozen cells up to 10−15 $\mu$m thick were with volumetric resolution of up to 60 nm were acquired using synchrotron sources [17–19] and images with volumetric resolution of up to 100 nm were were acquired using laboratory laser-plasma sources [20–22].

Microscopes also see a rapid development in the EUV range. They are used to obtain $2D$ images of dried cells, as well as masks for EUV lithographs [12,13]. For instance, an image of a Chrisodidymus silicon cell was obtained with a lateral resolution of about 50 nm in Ref. [14]. An image of CT26 fibroblast cells and diatoms with a lateral resolution of about 100 nm was acquired in Ref. [15]. The structure of a mouse brain slice with a resolution of about 200 nm was studied in Ref. [16]. Supercoiled plasmid DNA images were obtained in Ref. [23].

At the moment, soft X-ray (SX) microscopy penetrates and strengthens its position in the arsenal of biology and healthcare. The hemoglobin content was analyzed in Ref. [24] at different stages in red blood cells infected with malaria plasmodium. B cells of the human immune system are studied in Ref. [20]. The effects of the SARS-CoV-2 virus on human cells were studied in Ref. [25]: immediately after infection, then after 6 h and after 24 h, while the cells are chemically fixed and frozen at different stages of virus development [26], so that they can withstand the dose of $10^7-10^8$ Gy.

The lateral resolution of SX-microscopes can reach $7-10$ nm [27–29], while the volume resolution, as shown above, is several times worse. The main factor limiting $3D$-resolution in SX-microscopes on Fresnel zone plates is the large depth of focus forcing to use technically complex angular tomography to restore the bulk structure of samples. The limited number of angular projections (due to the increasing path of rays through the sample at sliding lighting angles, which leads to signal attenuation), as well as the sample decenter during angular scanning, also affect $3D$-resolution [20,25].

The use of multilayer X-ray mirrors of normal incidence instead of Fresnel zone plates makes it possible to increase the numerical aperture of projection lenses. In this case, the DOF (depth of focus) can also be reduced by an order of magnitude and for $\mathrm{NA} = 0.3$, and the wavelength of $\lambda = 3$ nm it will amount to

$$\mathrm{DOF} \approx \lambda/\mathrm{NA}^2 = 33\,\mathrm{nm}. \quad (1)$$

From a practical point of view, this means that a sample slice with a thickness of $\pm 33$ nm will make the largest contribution to the generated image on the detector. Therefore, as in the case of confocal microscopy, it is possible to switch from angular to $z$-tomography and restore $3D$-structure by a series of projections along the sample axis [30].

The lateral resolution for incoherent lighting $\delta x$ is

$$\delta x = 0.61\lambda/\mathrm{NA} = 6\,\mathrm{nm}, \quad (2)$$

which is still significantly better than the longitudinal resolution. However, this problem of $z$-tomography can be solved later by $z$-imaging at two or three angles.

The extremely high requirements for the roughness and shape accuracy of mirror substrates is the main obstacle for the development of high-power soft X-ray microscopy based on multilayer normal-incidence mirrors. The aberration coefficient of the projection lens should not exceed $\lambda/14$ to ensure the diffraction quality of images according to the Marechal criterion. This corresponds to approximately 0.2 nm in the „water transparency window“. As our calculations and practice show, by taking into account the point scattering function reconstructed from the measured lens aberrations, diffraction image quality can also be obtained for aberrations at the level of $\lambda/4$, i.e. up to 0.8 nm for a wavelength of 3.37 nm from the „water transparency window“ and $1.1-1.5$ nm for wavelength $4.5-6$ nm from the „carbon transparency window“.

At present, primarily due to the development of EUV lithography, there is significant progress in the technology of manufacturing high-precision mirrors, in particular, ZEISS has achieved substrate manufacturing accuracy at the level of $\mathrm{RMS} = 0.1-0.2$ nm [31]. The results of the authors are inferior to these results and amount to the RMS value at the level of $0.6-0.8$ nm [32], which is nevertheless sufficient to create a high-resolution microscope lens. The data on advanced manufacturing methods and characterization of high-precision substrates can be found in Ref. [33], the data on ion-beam aspherization and shape correction of optical substrates for mirrors can be found in Ref. [34]. This result allowed manufacturing and putting into operation a microscope with a wavelength of 13.84 nm with a 46-fold magnification and study its resolution [35]. This paper briefly describes the microscope and presents the results of studying samples at three wavelengths of 13.84, 200,and 535 nm. Correlation analysis of images at different wavelengths provides new information about the object.

## 1. Operating principle of the microscope

IPM RAS created a laboratory microscope in 2021 with an operating wavelength of 13.84 nm and a magnification of $\times 46$ for studying biological samples,which uses a Schwarzschild lens as imaging optics [35]. An axial tomography technique was developed to study the volume structure of samples with a lateral resolution of 140 nm (1 pixel) and an axial resolution of up to 420 nm (3 pixels). The microscope has the following advantages due to replacement of the zone plate with a mirror lens:

1) the ability to perform axial tomography of samples, which does not require adding markers to the sample for alignment and adjustment when the sample shifts along the optical axis to obtain a three-dimensional image;

2) there is a possibility of accurate interferometric determination of the point scattering function (PSF) of the microscope, which then participates in image reconstruction;

3) mirror achromatism allows building an image in three different ranges: EUV ($\lambda = 13.84$ nm), UV ($\lambda_{mean} \approx 200$ nm) and in the visible spectrum. The wavelength is selected by changing the sources. A white LED is used ($\lambda_{mean} = 535$ nm) when working in an air

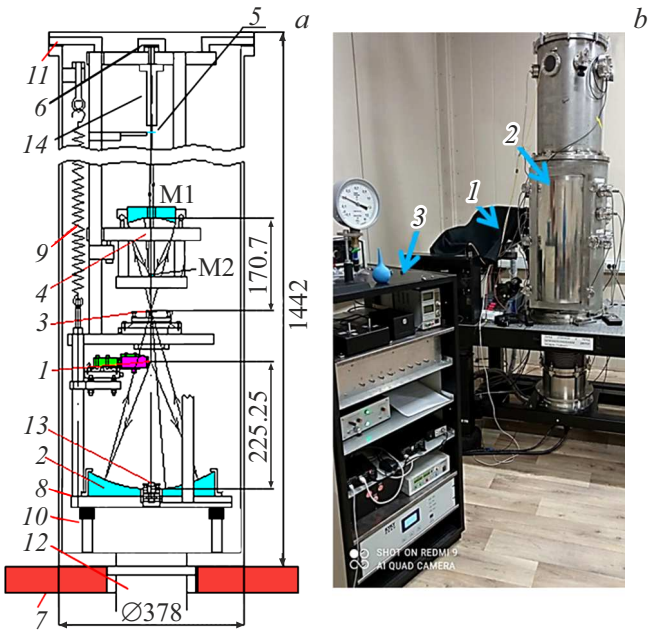


**Figure 1.** *a* — diagram of the microscope: *1* — source (laser-plasma or LED), *2* — collector mirror with a multilayer coating reflecting visible light and 13.84 nm, *3* — sample on a table with scanning along the vertical axis (due to a piezoactuator with feedback), *4* — dual-mirror Schwarzschild lens 46 x with aspheric primary mirror and multi-layer Mo/Si coating, *5* — multi-layer Mo/$ZrSi_2$filter on a ring with controlled insertion into the optical beam, *6* — matrix CMOS detector sensitive to soft X-ray range and cooled by a Peltier element with a water circuit, *7* — optical table, *8* — whatnot for optics, *9* — spring suspension to reduce the influence of optical vibrations, *10* — feet with rubber supports, *11* — anti-sway locks, *12* — vacuum pumping system, *13* — adjustment laser, *14* — lens hood; *b* — photo of the microscope: *1* — pulsed IR laser for generating radiation in a laser-plasma source, *2* — vacuum chamber, *3* — instrument rack.

environment. The radiation generated by irradiation of a gas jet exiting a conical supersonic nozzle *1* (Fig. 1) [36,37] by pulsed focused IR laser Ekspla NL303HT is used in case of operation in the vacuum. The input-output of a multilayer Mo/$ZrSi_2$filter *5* (Fig. 1) is provided which cuts off long-wave radiation ($T(\lambda = 20-1064\,\text{nm}) < 0.1\%$, $T(\lambda = 10.6\,\mu\text{m}) < 0.1\%$) and transmits $\lambda = 12.5-18\,\text{nm}$ radiation with a transmission coefficient of $T > 45\%$ [38]. At the same time, the lens *4* is the same, so the position of the sample *3* does not change, which means that images of the same sample regions can be unambiguously compared at different wavelengths.

A controlled shift of the sample is performed on a CoreMorrow piezoceramic actuator along the optical axis at a distance of up to $40\,\mu\text{m}$ in increments of up to 1 nm for obtaining three-dimensional images in a microscope. Due to the large numerical aperture of the lens (NA = 0.27), the sample section located in the subject plane is projected onto matrix detector GPixel 2020BSI PulSar rather sharply, which allows performing the so-called axial, or $z$-tomography. A set of images, i.e. a series of sections with different depths of occurrence in the sample thickness, is acquired by shifting the sample along the optical axis. The exposure time of one frame at 13.84 nm was 1–7 s depending on the thickness and type of sample, 214 frames with a stepout along $z$ $0.14\,\mu\text{m}$ and a time of up to 25 min were required for acquiring a series of frames along the thickness of the sample.

## 2. Measurement and accounting of the scattering function of a microscope point

We apply the deconvolutionary image reconstruction described in Ref. [35] for eliminating the impact of out-of-focus layers on images and to obtain clear three-dimensional images. Taking into account the three-dimensional PSF in such a microscope is very important, since even a nanometer error in the shape of mirrors (in terms of the root-mean-square deviation from the calculated shape) for so short wavelengths ($\lambda = 13.84\,\text{nm}$) affects the PSF. This results in blurring of the image on images recorded on the matrix, but the blurring effect can be significantly reduced after solving the inverse problem (deconvolution).

We obtained a three-dimensional PSF of the microscope taking into account the actual shape of the mirrors in two stages: we recorded the aberrations of the objective, and then modeled the PSF based on them in the Zemax program. We used a point diffraction interferometr (PDI) of our proprietary design [39] based on a spherical fiber source with an aperture narrowed to subwavelength dimensions ($d \approx 250\,\text{nm}$) and angular aberrations in the numerical aperture NA = 0.27 (coinciding with NA of the lens) [40]. The source installed in the object plane of the lens *1* (Fig. 2, *a*) was powered with the light of 632.8 nm phase-stabilized He–Ne laser. The divergent spherical front of the source was reflected from the mirrors of the lens, gaining aberrations caused by a residual error in the shape of the mirrors (after ion-beam correction on the $\text{RMS}_{\text{aberration}} = \lambda/5$ at $\lambda = 13.84\,\text{nm}$ [38]), and was focused in the image plane of the lens, where the second spherical wave source *2* was placed (Fig. 2, *a*), which is coherent with the first source. Then these two beams, the working beam and the reference beam, were projected onto the matrix detector with a lens. The lens formed a clear image of the M1 mirror with an interferogram superimposed on it. Lens aberrations were determined by the bending of the interference fringes. The resulting PSF has the form of a double light cone and is close to diffraction-limited at the wavelength of 13.84 nm, because the aberrations are small, at the level of $\lambda/5$. The PSF caustic has a height of $0.8\,\mu\text{m}$ and a diameter of about $0.14\,\mu\text{m}$, i.e. each point of the sample in the lateral plane is blurred by about 1 pixel, and by 8 pixels in the direction along the optical axis. This image blurring can be significantly reduced by making a three-dimensional

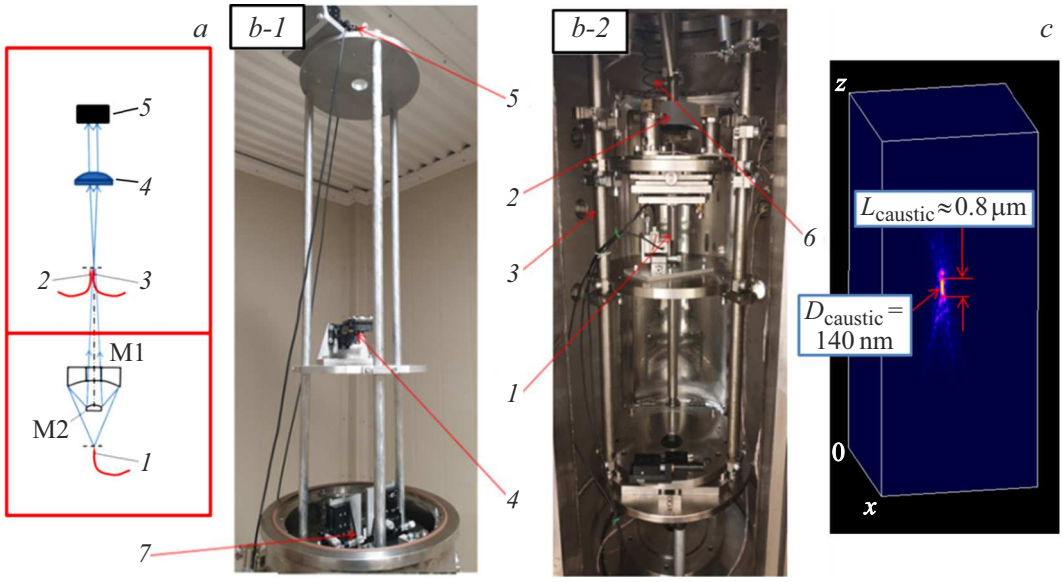


**Figure 2.** Scheme for measuring the aberrations of the Schwarzschild lens on the PDI. *a* — *1* — single-mode spherical fiber source with sub-wave output aperture (SSW № 1), *2, 3* — fiber source with 5 um aperture (SSW № 2 and № 3), *4* — lens, *5* — matrix detector; *b* — *1, 2* — photo of the built-in interferometer in the microscope: *1* — SSW № 1, *2* — measured lens, *3* — optical shelf of the microscope, *4* — lens for imaging the primary mirror of the lens with superimposed interferogram, *5* — matrix detector, *6* — spring suspension to reduce the impact of external vibrations on interferogram, *7* — single-mode fiber chips (SSW № 2 and № 3); *c* — volume scattering function of a point with a microscope, taking into account the measured lens aberrations ($\lambda = 13.84$ nm).

deconvolution of the image, taking into account the features of PSF, in the ImageJ program with DeconvolutionLab2 plugin [2].

## 3. Acquisition of microscopic images at different wavelengths

The resolution of the microscope was estimated at the shortest wavelength of 13.84 nm, since in this case the diffraction blur is minimal ($0.61\lambda/\mathrm{NA} \approx 30$ nm for $\mathrm{NA} = 0.27$) and much smaller than the projection of the 6.5-micron detector pixel into the sample plane ($6.5\,\mu$m/46 (magnification) $\approx 140$ nm).

The sample was a suspension of $CeO_2$ polishing powder with $0.3-0.6\,\mu$m granules, and the substrate was a polyvinyl formaldehyde film with high transmission in the EUV range.

The image shows that not all the film is in focus of the lens due to its sagging. Granules of size $0.3-0.6\,\mu$m (the size was previously determined on an electron microscope) are most clearly imaged in the area along the diagonal of the frame that comes into focus. The cross-section (Fig. 3, *a*) shows that the $0.3\,\mu$m granule was represented as 0.42-micron, and the blur level of 20–80% of the signal was 1 pixel $= 0.14\,\mu$m.

Figure 4 shows a three-dimensional image of a fixed cell from a lily-of-the-valley stem obtained on the EUV. This is a standard sample for fluorescence microscopy, only with the coverslips removed [41]. It is possible to see the cell wall and intracellular structures.

Much attention was paid to correlation microscopy, when the same area was studied on the developed microscope in three wavelength ranges: with illumination by a photodiode in visible light ($\lambda_{mean} = 535$ nm), with illumination by laser-plasma source (LPS) radiation without a multilayer filter when the sample is mainly illuminated by UV radiation with an average wavelength of $\lambda_{mean} \approx 200$ nm and with the use of a filter ($\lambda = 13.84$ nm). The same region was then examined using an scanning electron microscope EM-1400 (SEM) (Jeol, Japan).

Images of the mouse femur section were obtained (Fig. 5) and the most interesting areas for comparison were selected (Fig. 6). The EUV and UV resolution is comparable to the SEM resolution for this magnification (46x). The contrast of EUV images is attributable to absorption, the contrast of UV images is attributable to absorption and refraction at the boundaries of matter, the contrast of visible light images is attributable to refraction. The SEM image is constructed by detecting secondary electrons generated under the influence of a scanning electron beam. The efficiency of secondary electron emission is higher the greater the angle of incidence of the scanning beam on the surface of the object under study, in other words, inclined surfaces are brighter than horizontal ones, and therefore axially thin and flat structures are depicted by SEM in low contrast (Fig. 5, *c* and 6, *c*), in contrast to their UV and EUV images (Fig. 5, *a, b* and 6, *a, b*). Axially thin ($H = 150-300$ nm) regions (shown by dotted lines in Fig. 6) are clearly drawn on the EUV, but hardly noticeable

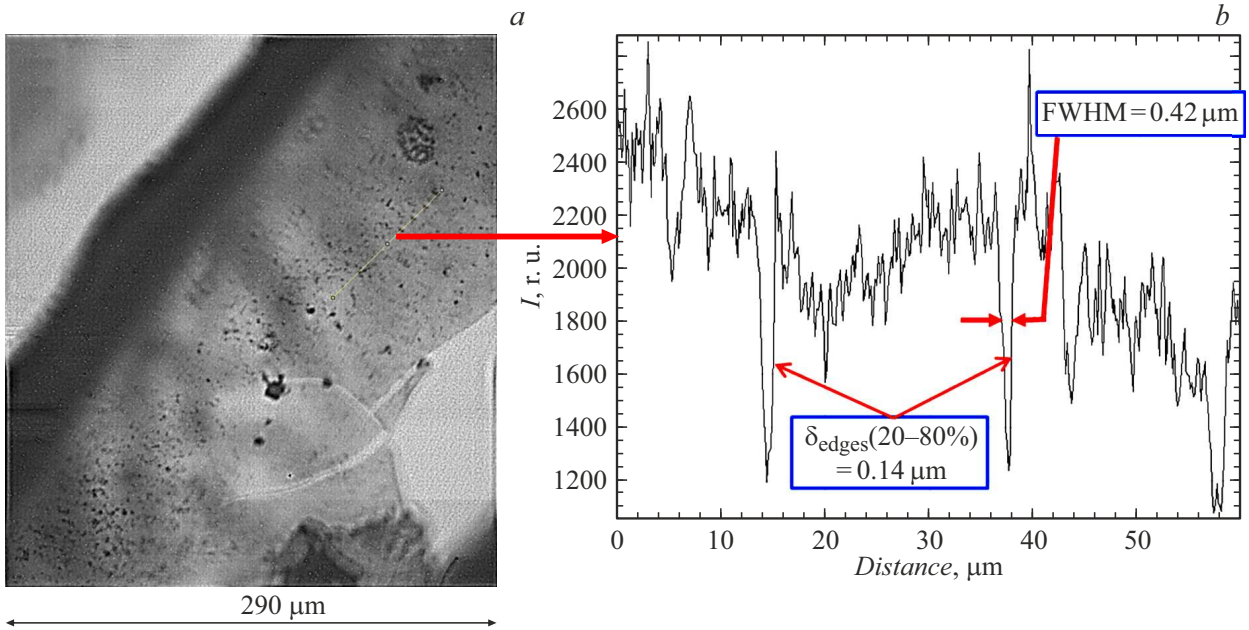


**Figure 3.** *a* — image of polishing powder $CeO_2$ with granules of size $0.3-0.6\,\mu$m on a polyvinyl formaldehyde film ($\lambda = 13.84$ nm); *b* — cross-section of granules in the focal region.

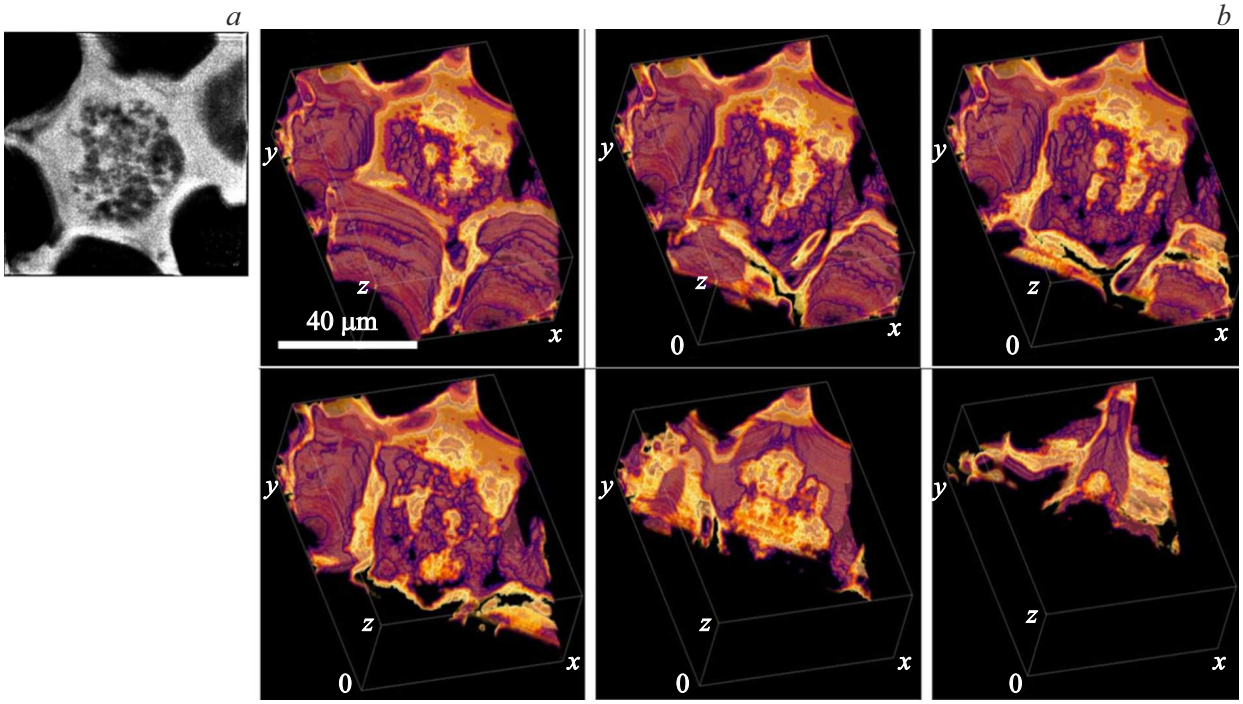


**Figure 4.** Images of lily-of-the-valley stem cell obtained at $\lambda = 13.84$ nm: *a* — one of the observed slices; *b* — a series of diagonal slices of the reconstructed volume cell.

on the UV and SEM. In the EUV (Fig. 6, *b*), the bone walls are 20–50% narrower than in the UV (Fig. 6, *a*), which is associated with a decrease of diffraction blur images at a wavelength reduction of 15 times (from 200 to 13.84 nm). See the Appendix for more information about preparation of a mouse bone slice.

Figure 7 shows a cross-section image of a rat lung. The contrast in the UV image is to a lesser extent attributable to the absorption of light in matter, and to a greater extent is attributable to the refraction. Rays at the boundaries of structures are refracted and enter the lens at an angle, as a result of which in UV images the boundaries of structures

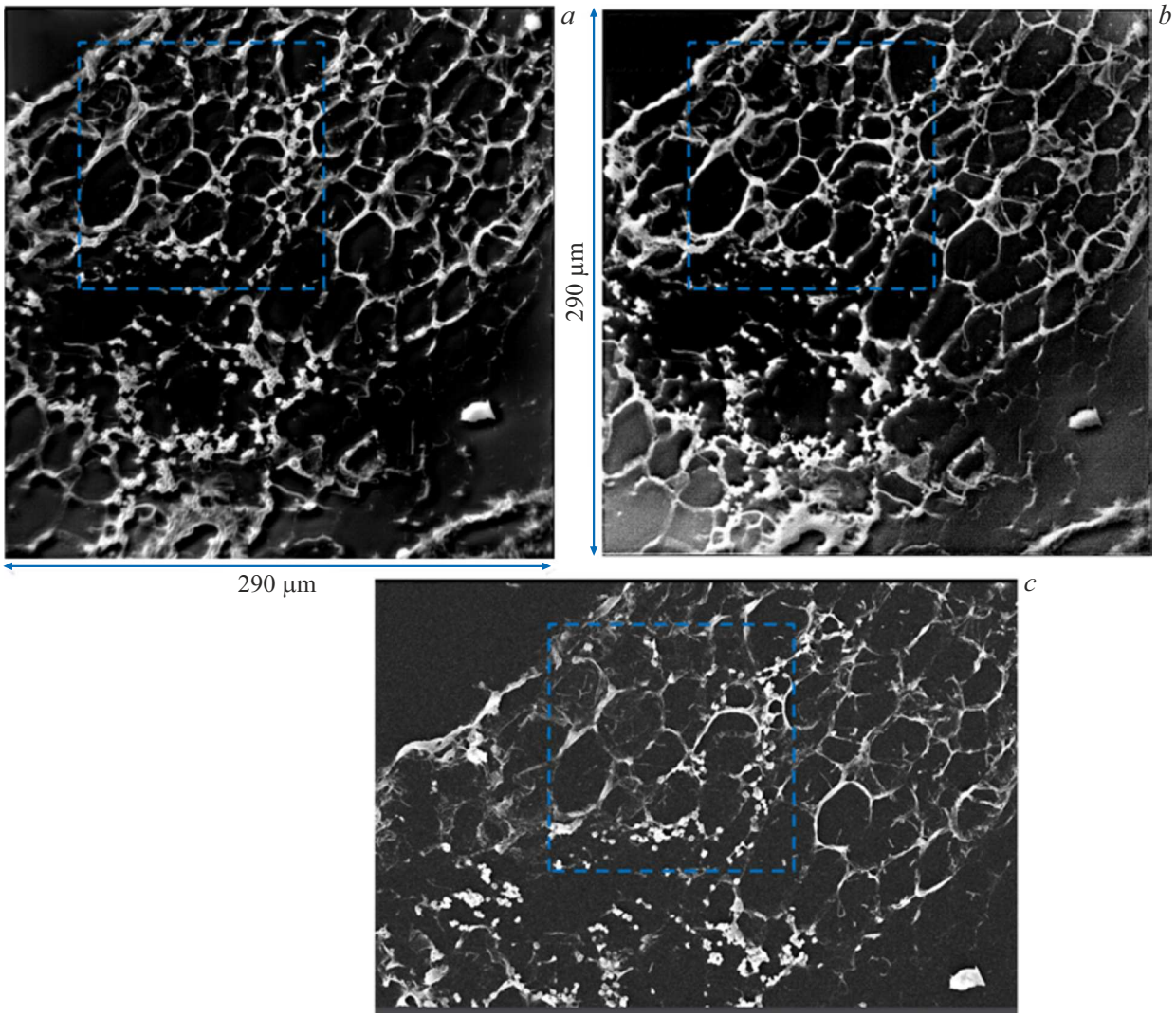


**Figure 5.** Cross-section of the mouse femur at different wavelengths: *a* — UV, *b* — EUV, *c* — SEM (the blue dotted square shows the area for comparison). The color is inverted for better perception.

look darker than their centers (Fig. 7, *b*). The contrast in EUV is only attributable to absorption, so there are no such edge artifacts (Fig. 7, *a*). The absorption on the EUV is stronger than on the UV, so the axially thin structures that are gray in the UV are colored black in the EUV. We see diffraction blurring in visible light (Fig. 7, *c*) caused by a large wavelength and the predominance of refraction over absorption, and, as a result, large black artifacts at the edges of the structures. The sample preparation is described in the Appendix.

The resolution of the EUV exceeds the resolution of visible light because of a shorter wavelength, and, as a result, weaker blurring due to diffraction, which is clearly visible in the image 8), where a clearer image was obtained at 13.84 nm than in visible light.

The sample preparation is described in the Appendix.

Another interesting object was a section of primary mouse hippocampal cells on the 18th day of development *in vitro* (Fig. 9). Cell cultures were pre-fixed with 2.5% glutaraldehyde and osmium tetradoxide, dehydrated in an increasing concentration of ethanol, and then Polymerized in a mixture of Epon-based resins 812. Sections with a thickness of 0.5 $\mu$m were obtained using Leica UC7 ultramicrotome. Sample preparation protocols are given in the Appendix. The EUV and visible light image of cells were acquired. The EUV image is much clearer, it was possible to see the shape of the cell, the cell nucleus, the ratio of the nucleus/cytoplasm and the cell matrix.

Another interesting effect was found when studying sections of the mouse retina on an EUV microscope before and after finding the sample under an electron beam in a transmission electron microscope (Fig. 10). When irradiated in an electron microscope, light atoms whose bond strength with carbon is weaker than the strength of carbon-carbon bonds (mainly oxygen and nitrogen) are knocked out of the preparation under the action of an electron beam. Heavy

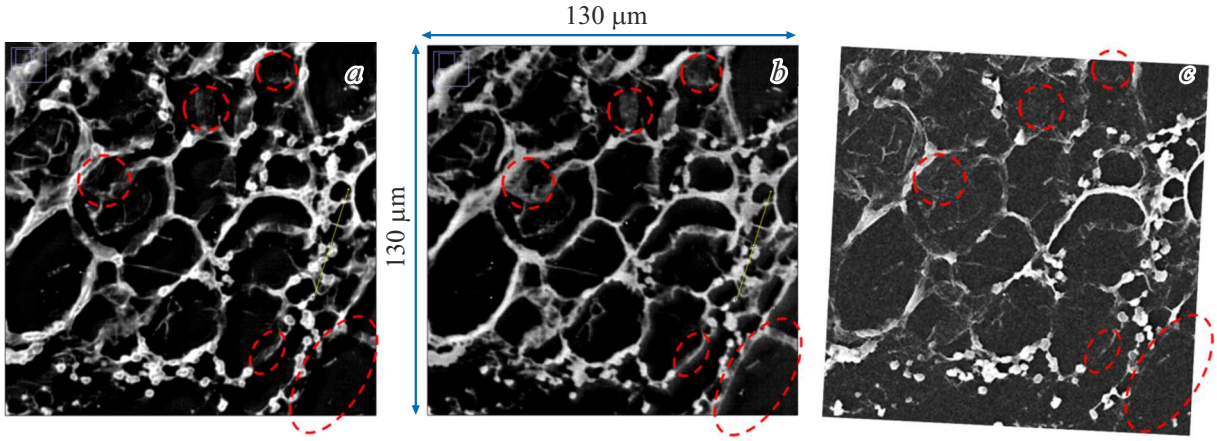


**Figure 6.** Area for comparison in a mouse femur section at different wavelengths: *a* — UV, *b* — EUV, *c* — SEM. Red dotted circles / ovals indicate areas where the difference between these visualization methods is more clear.

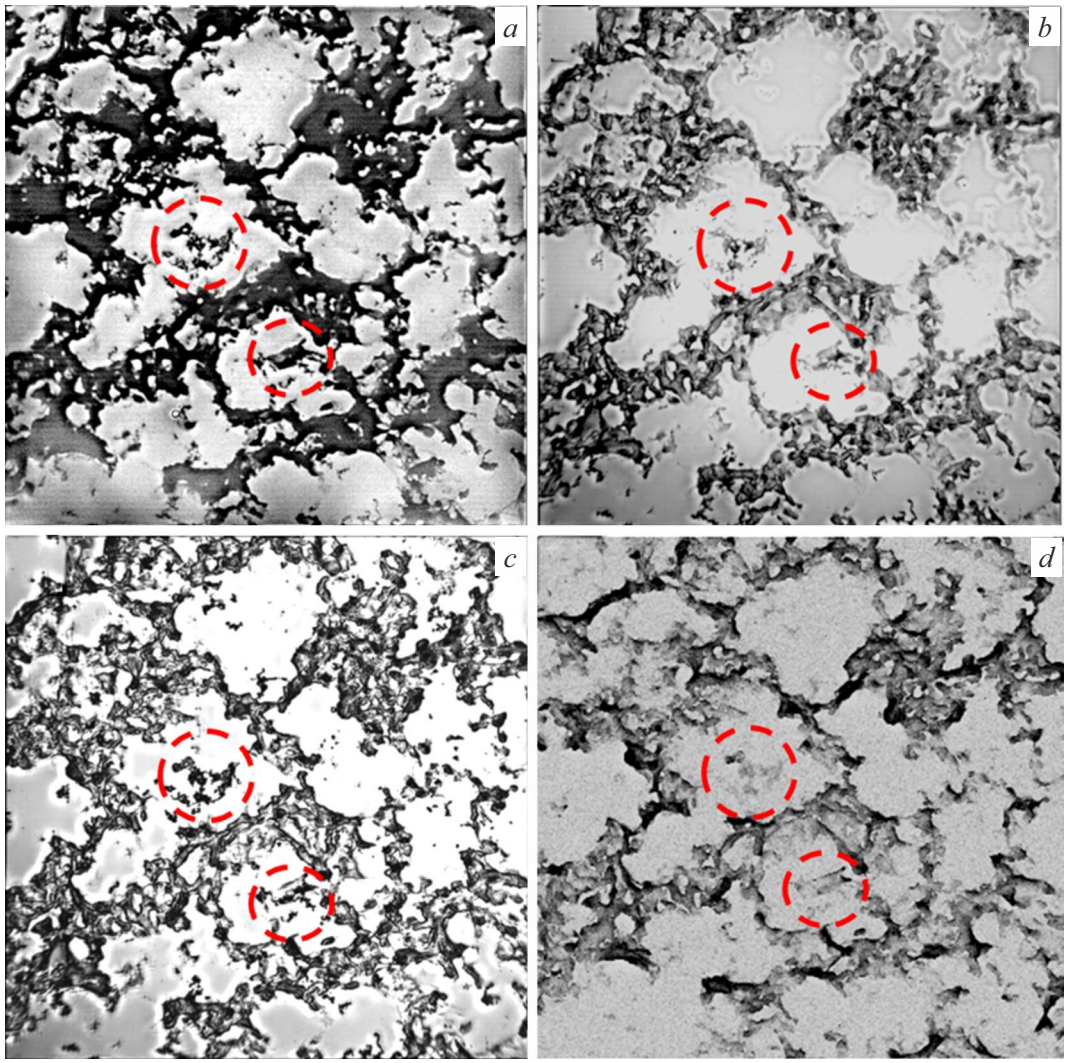


**Figure 7.** Rat lung section: *a* — EUV image ($\lambda = 13.84$ nm), *b* — UV image ($\lambda_{mean} \approx 200$ nm), *c* — in visible light ($\lambda_{mean} = 535$ nm), *d* — SEM image. Slice thickness 15 $\mu$m, field of view $130 \times 130$ $\mu$m.

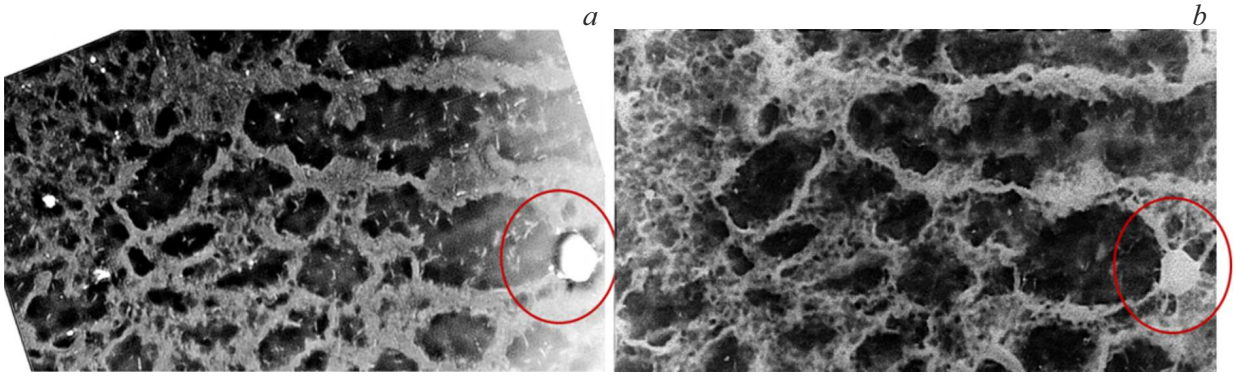


**Figure 8.** Section of a decellularized mouse lung matrix of size $230 \times 115 \times 6\,\mu$m on the EUV ($a$) and in the same visible light microscope ($b$).

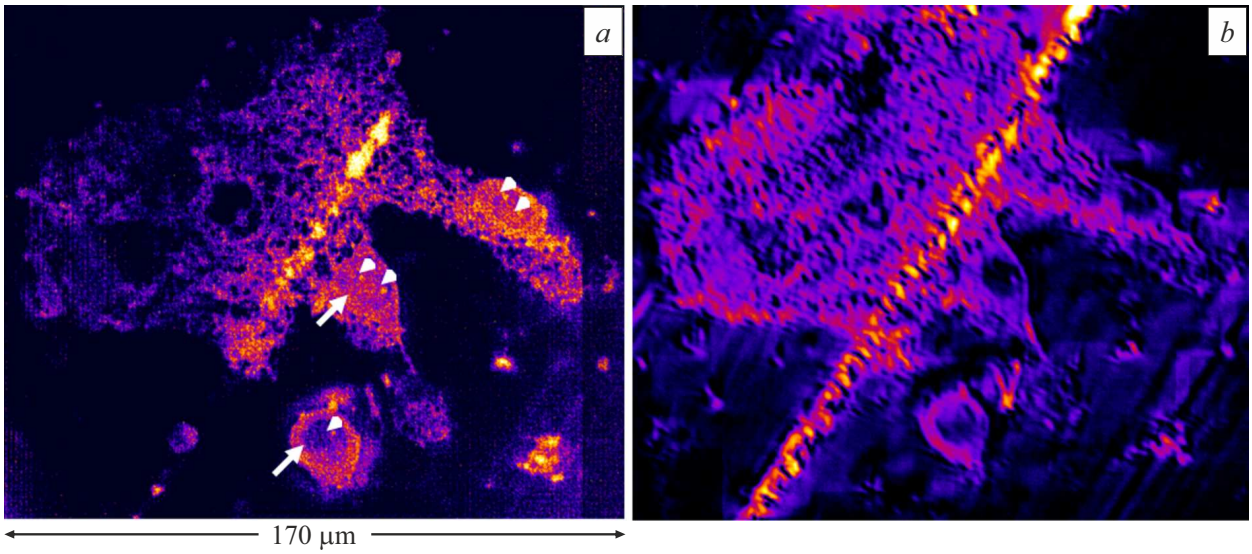


**Figure 9.** Section of primary mouse hippocampal cells with a thickness of $0.5\,\mu$m, the tissue is embedded in the EUV-transparent resin Epon 812: $a$ — at 13.84 nm from a laser-plasma source, $b$ — in visible light from LED / diode source. Arrows — kernels, pointers — kernels. Bright streak — knife mark.

osmium metal atoms that are chemically bound to carbon (mainly by double bonds of fatty acid residues in lipid membranes after the staining procedure) remain in the preparation, so places with a high content of carbon and metal appear more contrast in the image.

Samples should be of two types for good quality EUV images. First type— fabrics with a pronounced cellular structure, with a thickness of about $5-25\,\mu$m. For them, a contrast is obtained due to jumps in the density of the substance. Such slices are cut in paraffin, and then it is removed. Second type — pore-free fabrics cut into layers with a thickness of $0.2-0.5\,\mu$m, with osmium-contrasted membranes, in EUV-transparent for resin Epon 812. Osmium fixation is necessary to increase the contrast of carbon, with which osmium binds effectively. Contrast increases due to a decrease of the depth of penetration of EUV radiation into metallic osmium.

## Conclusions

The correlation microscopy is implemented on the developed mirror EUV microscope with $z$-tomography when one field on the sample is taken at three wavelengths: at 13.84 nm (EUV), at 200 nm (UV) and at 535 nm (visible light).

The advantage of resolution in the EUV range over visible light and UV microscopy was demonstrated. The main advantage of EUV over UV, SEM, and optical images is that the contrast is generated by absorption, so the axially fine features on the EUV are clearly visible. Also, compared to UV and visible light on the EUV, the resolution almost does not suffer from diffraction blurring.

In general, it can be seen that the $z$-tomography method in EUV microscopy works well, but a larger magnification is required to obtain a better resolution, so now work is

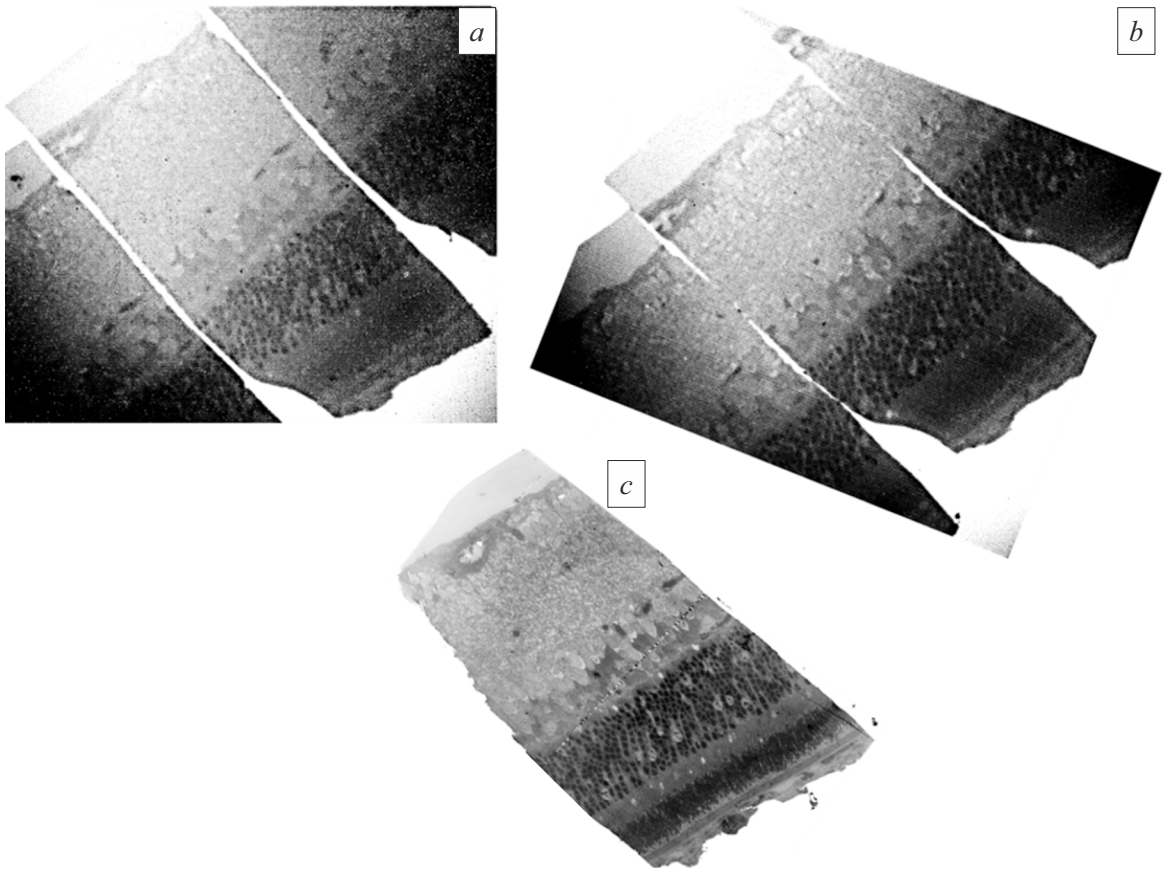


**Figure 10.** EUV image of a rat retinal slice: *a* — unirradiated by an electron microscope; *b* — irradiated; *c* — TEM image of a similar slice. Cut-off thickness 200 nm, field of view 260 × 220 $\mu$m.

underway for creation of a 345x EUV microscope. Work is also underway for creation of a lens for a shorter wavelength range.

### Acknowledgments

The work was performed with the support of the Russian Science Foundation № 22-62-00068 and with use of equipment of the Common Research Center „Physics and technology of micro- and nanostructures“ at the Institute for Physics of Microstructures of the Russian Academy of Sciences. Part of the work was performed using equipment purchased under the development program MSU PNR5.13. Brain cells were prepared with the participation of the PRMU Correlation Microscopy Center.

### Conflict of interest

The authors declare that they have no conflict of interest.

## References

[1] E. Hanssen, Ch. Knoechel, M. Dearnley, M.W.A. Dixon, M. Le Gros, C. Larabell, L. Tilley. J. Struct. Biol., **177**, 224 (2012). DOI: 10.1016/j.jsb.2011.09.003

[2] D. Sage, L. Donati, F. Soulez, D. Fortun, G. Schmit, A. Seitz, R. Guiet, C. Vonesch, M. Unser. Methods, **115**, 28 (2017). DOI: 10.1016/j.ymeth.2016.12.015

[3] L. Schermelleh, R. Heintzmann, H. Leonhardt. J. Cell Biol., **190** (2), 165 (2020). DOI: 10.1083/jcb.201002018

[4] V. Lučić, A. Rigort, W. Baumeister. J. Cell Biol., **202** (3), 407 (2013). DOI: 10.1083/jcb.201304193

[5] K. Leigh, P. Navarro, S. Scaramuzza, W. Chen, Y. Zhang, D. Castaño-Díez, M. Kudryashev. Methods Cell Biol., **152**, 217 (2019).

[6] M. Kördel, A. Dehlinger, C. Seim, U. Vogt, E. Fogelqvist, J.A. Sellberg, H. Stiel, H.M. Hertz. Optica, **7** (6), 658 (2020). DOI: 10.1364/OPTICA.393014

[7] B. Rösner, F. Koch, F. Döring, V.A. Guzenko, M. Meyer, J.L. Ornelas, A. Späth, R.H. Fink, S. Stanescu, S. Swaraj, R. Belkhou, B. Watts, J. Raabe, C. David. Microsc. Microanal., **24**, 272 (2018).

[8] I. Kounatidis, M.L. Stanifer, M.A. Phillips, P. Paul-Gilloteaux, X. Heiligenstein, H. Wang, Ch.A. Okolo, Th.M. Fish, M.C. Spink, D.I. Stuart, I. Davis, S. Boulant, J.M. Grimes, I.M. Dobbie, M. Harkiolaki. Cell., **182** (2), 515 (2020). DOI: 10.1016/j.cell.2020.05.051I

[9] A. Gianoncelli, V. Bonanni, G. Gariani, F. Guzzi, L. Pascolo, R. Borghes, F. Billé, G. Kourousias. Appl. Sci., **11** (16), 7216 (2021). DOI: 10.3390/app11167216

[10] T. Parkman, M. Nevrkla, A. Jančárek, J. Turňová, D. Pánek, M. Vrbová. Appl. Sci., **10** (18), 6373 (2020). DOI: 10.3390/app10186373

[11] I. A. Artyukov, A.V. Vinogradov, E. A. Bugaev, A. Yu. Devizenko, V. V. Kondratenko, Yu. S. Kasyanov. ZhETF, **136** (5), 1009 (2009). (in Russian).
[12] M. Toyoda, K. Yamasoe, T. Hatano, M. Yanagihara, A. Tokimasa, T. Harada, T. Watanabe, H. Kinoshita. Appl. Phys. Express., **5** (11), 112501 (2012). DOI: 10.1143/APEX.5.112501
[13] L. Juschkin, R. Freiberger, K. Bergmann. J. Phys.: Conf. Ser., **186**, 012030 (2009).
[14] A. Torrisi, P. Wachulak, Ł. Węgrzyński, T. Fok, A. Bartnik, T. Parkman, Š. Vondrova, J. Turvňova, B.J. Jankiewicz, B. Bartosewicz, H. Fiedorowicz. J. Microscopy, **00** (0), 1 (2016). DOI: 10.1111/jmi.12494A
[15] P.W. Wachulak, A. Torrisi, A. Bartnik, Ł. Węgrzyński, T. Fok, H. Fiedorowicz. Appl. Phys. B, **123**, 25 (2017). DOI: 10.1007/s00340-016-6595-5
[16] T. Ejima, F. Ishida, H. Murata, M. Toyoda, T. Harada, T. Tsuru, T. Hatano, M. Yanagihara, M. Yamamoto, H. Mizutani. Opt. Express, **18** (7), 7203 (2010). DOI: 10.1364/OE.18.007203
[17] P.A.C. Takman, H. Stollberg, G.A. Johansson, A. Holmberg, M. Lindblom, H.M. Hertz. J. Microscopy, **226**, 175 (2007).
[18] C.A. Larabell, M.A. Le Gros. Molec. Biol. Cell, **15**, 957 (2004).
[19] D. Weib, G. Schneider, B. Niemann, P. Guttmann, D. Rudolph, G. Schmah. Ultramicr., **84**, 185 (2000).
[20] M. Bertilson, O. von Hofsten, U. Vogt, A. Holmberg, A.E. Christakou, H.M. Hertz. Opt. Lett., **36** (14), 2728 (2011). DOI: 10.1364/OL.36.002728
[21] E. Fogelqvist, M. Kördel, V. Carannante, B. Önfelt, H.M. Hertz. Sci. Rep., **7**, 13433 (2017).
[22] H.M. Hertz, O. von Hofsten, M. Bertilson. J. Str. Biol., **177** (2), 267 (2012).
[23] P.W. Wachulak, A. Torrisi, A. Bartnik, L. Wegrzynski, T. Fok, H. Fiedorowicz. J. Phys.: Conf. Ser., **849**, 012050 (2017). DOI: 10.1088/1742-6596/849/1/012050
[24] E. Hanssen, C. Knoechel, M. Dearnley. J. Struct. Biol., **177**, 224 (2012).
[25] V. Loconte, J.-H. Chen, M. Cortese, A. Ekman, M.A. Le Gros, C. Larabell, R. Bartenschlager, V. Weinhardt. Cell Reports Methods, **1** (7), 100117 (2021). DOI: 10.1016/j.crmeth.2021.100117
[26] J.-H. Chen, B. Vanslembrouck, V. Loconte, A. Ekman, M. Cortese, R. Bartenschlager, G. McDermott, C.A. Larabell, M.A. Le Gros, V. Weinhardt. STAR Protocols, **3** (1), 101176 (2022). DOI: 10.1016/j.xpro.2022.101176
[27] B. Rösner, F. Koch, F. Döring, V.A. Guzenko, M. Meyer, J.L. Ornelas, A. Späth, R.H. Fink, S. Stanescu, S. Swaraj. Microsc. Microanalysis, **24**, 270 (2018). DOI: 10.1017/S1431927618013697
[28] W. Chao, P. Fischer, T. Tyliszczak. Opt. Express, **20**, 9777 (2012).
[29] V. De Andrade, V. Nikitin, M. Wojcik. Adv. Mater., **33**, 2008653 (2021).
[30] I.V. Malyshev, N.I. Chkhalo. Ultramicroscopy, **202**, 76 (2019).
[31] Electronic source. Available at: https://www.euvlitho.com/2018/P22.pdf
[32] N.I. Chkhalo, I.V. Malyshev, A.E. Pestov, V.N. Polkovnikov, N.N. Salashchenko, M.N. Toropov, A.A. Soloviev. Appl. Optics, **55** (3), 619 (2016). DOI: 10.1364/AO.55.000619
[33] N.I. Chkhalo, I.V. Malyshev, A.E. Pestov, V.N. Polkovnikov, N.N. Salashchenko, M.N. Toropov. UFN, **190** (1), 74 (2020) (in Russian). DOI: 10.3367/UFNr.2019.05.038601
[34] N.I. Chkhalo, I.A. Kaskov, I.V. Malyshev. Prec. Eng., **48**, 338 (2017).
[35] I.V. Malyshev, D.G. Reunov, N.I. Chkhalo. Opt. Express, **30** (26), 47567 (2022).
[36] A.N. Nechay, A.A. Perekalov, N.N. Salashchenko, N.I. Chkhalo. Opt. i spektr., **129** (2), 146 (2021) (in Russian).
[37] A.V. Vodop'yanov, S.A. Garakhin, I.G. Zabrodin, S.Yu. Zuev, A.Ya. Lopatin, A.N. Nechay, A.E. Pestov, A.A. Perekalov, R.S. Pleshkov, V.N. Polkovnikov, N.N. Salashchenko, R.M. Smertin, B.A. Ulasevich, N.I. Chkhalo. Quantum Electron., **51**, 700 (2021). DOI: 10.1070/QEL17598
[38] N.I. Chkhalo, E.B. Kluenkov, A.Ya. Lopati et al. Thin Solid Films, **631**, 93 (2017).
[39] M. Toropov, N. Chkhalo, I. Malyshev, N. Salashchenko. Opt. Lett., **47** (14), 3459 (2022).
[40] A.A. Akhsakhalyan, N.I. Chkhalo, N. Kumar, I.V. Malyshev et al. Prec. Eng., **72**, 330 (2021).
[41] Electronic source. Available at: https://www.optics-pro.com/botany/lieder-convallaria-maigloeckchen-rhizom-quer-konzentrische-leitbuendel/p,64540
[42] A.D. Pospelov, O.M. Kutova, Y.M. Efremov, A.A. Nekrasova, D.B. Trushina, S.D. Gefter, E.I. Cherkasova, L.B. Timofeeva, P.S. Timashev, A.V. Zvyagin, I.V. Balalaeva. Cells, **12**, 2030 (2023). DOI: 10.3390/cells12162030

*Translated by A.Akhtyamov*

## Appendix

### 1. Preparation of a mouse femur section sample

The bones were placed in 10% neutralized formalin (Biovitrum, St. Petersburg, Russia) for 48 h at room temperature. They were then washed from excess fixative under running water for 20 min, and then placed for decalcification in Richman-Gelfand-Hill liquid (90 %formic acid, 38.8% hydrochloric acid, and distilled water) for 24 h. The decalcification endpoint was confirmed by a standard gravimetric test. The sample was then extracted from the acid solution under running water for 30 min and dehydrated in 5 replicates of modified isopropyl alcohol „Blik“ (produced by „Blikmedikl“, Taganrog, Russia) in accordance with the manufacturer's instructions. Bones were embedded in paraffin, and sections (2 sections for each sample) with a thickness of 8 $\mu$m were obtained using Epredia HM 325 microtome (Thermo Fisher Scientific, Waltham, MA, USA). The samples were dewaxed in xylene for 5 min before microscopy.

### 2. Preparation of rat lung section sample

Rat lung tissue samples (*Rattus norvegicus*, albino, nonlinear) were fixed with buffered formalin (4%), kept in 15% sucrose solution on phosphate buffer (4 h) and then in 30% solution sucrose on a phosphate buffer (8 h). The samples were then placed in a freeze-mould in a cryotomy medium for histological samples Tissue-Tek O. C. T. Compound. Rapid freezing was performed by immersing the mould in isopropyl alcohol at a temperature of $-80^{\circ}$C, keeping the isopropyl alcohol away from the sample surface. Sections with a thickness of 3–15 $\mu$m at a temperature of $-18^{\circ}$C were obtained using an 1850CM UV cryostat (Leica, Germany). Tissue sections were mounted on silicon nitride substrates pre-coated with polylysine, the cryomedium was removed, the samples were dehydrated by passing through a series of alcohols of increasing concentration and anhydrous acetone, and then dried at the critical point (CT) of carbon dioxide. In this state, the preparations are stable in vacuum and suitable for testing in UV/EUV modes.

For the SEM study, CT-dried preparations were additionally coated with a gold layer using an ion sputtering unit to impart electrical conductivity to the preparations and increase the efficiency of secondary electron generation. SEM images were obtained using JSM-6380 electron microscope (JEOL, Japan).

### 3. Preparation of a decellularized mouse lung matrix sample

Matrices were obtained according to the method described in Ref.[42]. The lungs of BALB/c mice were sequentially incubated in 0.5% Triton X-100 solution, then in 0.5% SDS solution, then in the solution of 1% sodium deoxycholate. Matrix samples were transferred to 10% neutralized histological formalin for 24 h at room temperature after decellularization was completed. Then they were washed from excess fixative under running water for 20 min and dehydrated in 5 replicates of modified isopropyl alcohol „Blik“ (BlikMediklProduction, Taganrog, Russia) in accordance with the manufacturer's instructions. Matrices were embedded in paraffin and sections (2 sections per 1 sample) with a thickness of 7 $\mu$m were prepared using Epredia HM 325 microtome (Thermo Fisher Scientific, USA). The samples were dewaxed in xylene for 5 min before microscopy.

### 4. Protocol for preparing a mouse hippocampal primary cell slice

- Primary fixation in 2.5% glutaraldehyde for 2 h in cacodylate buffer 0.15 M with 2 MMCCL2).
- Flushing for 5 × 3 min in cacodylate buffer 0.15 M with 2 $MmCl_2$ (room temperature).
- Postfix: 1 h, on ice; freshly prepared 0.3 M cacodylate buffer with 1% aqueous solution of osmium tetrachloride + 1.5% potassium ferrocyanide.
- Flushing: 5 × 3 min; dd $H_2O$ (double-distilled water).
- Dewatering: 2 × 15 min, on ice: 50, 70, 90, 100, 100%, acetone, dd $H_2O$.
- Encapsulation in Epon 818-based epoxy resins according to the manufacturer's recommendations for „solid“ resins:
- Epon 818 „solid“: acetone (1:3) 2 h.
- Epon 818 „solid“: acetone (1:1) 2 h.
- Epon 818 „solid“: acetone (3:1) 2 h.
- Epon 818 „solid“: 100% 37°C — 24 h.
- Epon 818 „solid“: 100% 45°C — 24 h.
- Epon 818 „solid“: 100% 60°C — 24 h.

### 5. Preparation of a rat retinal section sample

Tissue sections embedded in Epon 812 were prepared according to the TEM sample preparation protocol. In short, tissue samples were fixed with 2.5% glutaraldehyde solution in 100 mM sodium cacodylate solution, then lipid membranes were stabilized with 1% sodium cacodylate solution. osmium tetraoxides on the same buffer, they were dehydrated by passing through a series of alcohols of increasing concentration. The samples were impregnated with 2% uranyl acetate *en bloc* at the stage of 70% ethanol solution for adding an additional electron density to the protein component. The samples were converted to anhydrous acetone after 96% ethyl alcohol and impregnated with a mixture of acetone and Epon 812 epoxy resin (Spi-Pon 812, SPI Inc., USA), gradually increasing the resin concentration. After conversion to pure resin, the resin was polymerized at 55–60°C. Sections of the required thickness were made from the obtained moulds using Ultracut-E ultramicrotome (Reichert-Jung, Austria) provided with Ultra 45 diamond knife (Diatom, Switzerland). Sections were mounted on silicon nitride substrates for UV/EUV studies and on polyvinyl-formaldehyde films on standard copper grids with one cell for correlation EM/UV/EUV studies. JEM-1400 electron microscope (Jeol, Japan) with an accelerating voltage of 80 kV was used to acquire TEM images.